



## Facile synthesis of ultrasmall tin oxide nanoparticles embedded in carbon as high-performance anode for lithium-ion batteries

Qinghua Tian <sup>a</sup>, Yang Tian <sup>a</sup>, Zhengxi Zhang <sup>a,\*</sup>, Li Yang <sup>a,b,\*</sup>, Shin-ichi Hirano <sup>b</sup>

<sup>a</sup> School of Chemistry and Chemical Engineering, Shanghai Jiao Tong University, Shanghai 200240, PR China

<sup>b</sup> Hirano Institute for Materials Innovation, Shanghai Jiao Tong University, Shanghai 200240, PR China



### HIGHLIGHTS

- A composite of ultrasmall  $\text{SnO}_2$  embedded in carbon was prepared by a facile strategy.
- The peculiar structure brought the composite sufficient physical buffer ability.
- This composite ( $\text{SnO}_2/\text{C-59}$ ) exhibited an excellent electrochemical performance.

### ARTICLE INFO

#### Article history:

Received 26 April 2014

Received in revised form

12 June 2014

Accepted 2 July 2014

Available online 10 July 2014

#### Keywords:

Lithium-ion batteries

Anode materials

Ultrasmall tin oxide

Uniform distribution

### ABSTRACT

Tin oxide ( $\text{SnO}_2$ ) has received great attention as promising anode for lithium ion batteries because it offers a high theoretical capacity (ca.  $782 \text{ mAh g}^{-1}$  for  $\text{Li}_{4.4}\text{Sn}$ ) and a safe discharge potential versus  $\text{Li}/\text{Li}^+$  in comparison to commercialized graphite anodes, whereas it also suffer from the drawbacks of the huge volume change and low electronic conductivity during lithiation/delithiation processes. Herein, we have prepared a  $\text{SnO}_2/\text{C}$  composite of ultrasmall  $\text{SnO}_2$  nanoparticles (~6 nm and ~59.4% by weight) embedded in carbon matrix (denoted as  $\text{SnO}_2/\text{C-59}$ ) by a facile hydrothermal and subsequent carbonization approach. In this peculiar architecture, uniform distribution of  $\text{SnO}_2$ , and electronic conductivity of carbon matrix, which can effectively solve the problems of pulverization, loss of electrical contact and particle aggregation during cycling, therefore contributing to excellent lithium storage and cycling stability. A reversible capacity of  $839.1 \text{ mAh g}^{-1}$  is obtained at  $200 \text{ mA g}^{-1}$  after 217 cycles. More importantly,  $712.8 \text{ mAh g}^{-1}$  can be obtained at  $800 \text{ mA g}^{-1}$  even after 378 cycles.

© 2014 Elsevier B.V. All rights reserved.

### 1. Introduction

Tin oxide has attracted extensive interests in the context of energy storage and been considered as a promising alternative for commercial graphite anode due to its high theoretical capacity of  $782 \text{ mAh g}^{-1}$ , low toxicity, high abundance and safe working potential [1–4]. The theoretical capacity is two times higher than of commonly used graphite ( $372 \text{ mAh g}^{-1}$ ). And the safe working potential can effectively avoid the issues of easy presence of lithium plating during high current operation. Unfortunately, there are still obstacles that hinder the practical application of  $\text{SnO}_2$  anode materials for LIBs, such as severe pulverization and

capacity fading problems caused by the large volume variation (ca. 300%) during cycling process, subsequently resulting in loss of electrical conduct between adjacent particles [5]. To overcome these issues, several strategies have been employed to buffer the significant volume change such as fabricating novel  $\text{SnO}_2$  nano-structure electrode materials and designing composites with  $\text{SnO}_2$  and carbon nanomaterials [6,7]. For example, ultrathin  $\text{SnO}_2$  nanosheets [8], nanosheets assembled  $\text{SnO}_2$  hollow spheres [9],  $\text{SnO}_2$  nanotube arrays [10],  $\text{SnO}_2$  nanowires [11],  $\text{SnO}_2$  nanorods [12],  $\text{SnO}_2$  nanofibers and nanotubes with highly porous [13] and so forth have been synthesized to alleviate the absolute volume expansion of  $\text{SnO}_2$  electrodes during discharge/charge process. These peculiar architectures effectively shorten the lithium diffusion path, buffer the volume expansion and increase the contact interface between active materials and electrolyte, resulting in improved electrochemical performance, however, a certain amount of capacity fading still exists upon long-term cycling due

\* Corresponding authors. Tel.: +86 21 54748917; fax: +86 21 54741297.

E-mail addresses: [zhengxizhang@sjtu.edu.cn](mailto:zhengxizhang@sjtu.edu.cn) (Z. Zhang), [\(L. Yang\).](mailto:liyangce@sjtu.edu.cn)

to the breaking down, aggregation and pulverization of these  $\text{SnO}_2$  nanostructures [2].

Thus, design and fabrication of carbon supported  $\text{SnO}_2$  composites is considered to be another effectively strategy to alleviate the issues aforementioned, which integrates the advantages of carbon and  $\text{SnO}_2$  nanostructures [14]. Carbon materials, such as amorphous carbon [15], carbon nanotubes [16] and grapheme [17], have been regarded as the most promising choices for buffer matrixes, owing to their excellent buffering effect and high electronic conductivity.  $\text{SnO}_2$  combined with carbon to effectively accommodate the strain of volume change and avoid aggregation and pulverization [18]. Undoubtedly, the composites have been considered as promising anode candidates for lithium ion batteries (LIBs) and attracted great research interest worldwide. For example, carbon nanowires@ultrathin  $\text{SnO}_2$  nanosheets@carbon composite [19], CNTs@ $\text{SnO}_2$ @C coaxial nanocables [2], SWNTS@ $\text{SnO}_2$ @PPy coaxial nanocables [1],  $\text{SnO}_2$  nanosheets grown on graphene sheets [20], encapsulation of nanosized  $\text{SnO}_2$  particles in carbon nanotubes [21],  $\text{SnO}_2$ @carbon core-shell nanochains [22],  $\text{SnO}_2$ @C yolk-shell spheres [23] and  $\text{SnO}_2$ /graphene nanocomposites [24], all exhibiting high reversible capacities and improved electrochemical performances. However, these means alone only have limited improvement in lithium storage performance of  $\text{SnO}_2$ /carbon hybrid nanostructures. And the problems such as low tap density, complex preparation process and high cost of raw materials still exist. For the purpose of making the  $\text{SnO}_2$ /carbon hybrid nanostructures practical use in LIBs, great efforts still need to be done. Absolutely, there is a huge potential to synthesize and design  $\text{SnO}_2$ /carbon anode materials with better lithium storage performance for LIBs.

Herein, we prepared a  $\text{SnO}_2$ /C-59 composite by a simple hydrothermal and subsequent carbonization approach, avoiding special apparatus, tedious fabrication processes, toxic organic solvents, expensive raw materials and severe conditions. Firstly, we synthesized the  $\text{SnO}_2$ /carbonaceous polysaccharide precursor by using  $\text{Na}_2\text{SnO}_3 \cdot 4\text{H}_2\text{O}$  and D-glucose as the raw materials through simple hydrothermal process. Then, the  $\text{SnO}_2$ /C-59 composite was obtained by the  $\text{SnO}_2$ /carbonaceous polysaccharide precursor carbonization under Ar atmosphere. Observed by TEM, the  $\text{SnO}_2$  with average size of ca. 6 nm uniformly distributed in carbon matrix. The synergistic effect of ultrasmall  $\text{SnO}_2$  NPs, uniform distribution and electrically conductive carbon matrix, which providing  $\text{SnO}_2$ /C-59 composite with excellent electrochemical performance as an anode material for LIBs.

## 2. Experimental section

### 2.1. Preparation of samples

A typical preparation process was as follows:  $\text{SnO}_2$ /carbonaceous polysaccharide precursor was first synthesized by a simple hydrothermal approach: 0.35 g of  $\text{Na}_2\text{SnO}_3 \cdot 4\text{H}_2\text{O}$  (0.2 and 0.4 g were also investigated) and 1.2 g of D-glucose were dissolved in 14 mL of deionized water and stirred for 1 h. The solution was then transferred into a 25 mL Teflon-lined stainless steel autoclave, sealed, and kept at 180 °C for 8 h in an oven before cooling down to room temperature. Then, the product was harvested by centrifugation and washed with deionized water and ethanol. The as-prepared precursor was subsequently carbonization at a temperature of 500 °C for 3 h, under argon protective atmosphere at a ramping rate of 0.5 °C min<sup>-1</sup>. Finally, the  $\text{SnO}_2$ /C-59 composite was obtained. The sample prepared by using different mass of  $\text{Na}_2\text{SnO}_3 \cdot 4\text{H}_2\text{O}$  was labeled at three different contents of  $\text{SnO}_2$  in  $\text{SnO}_2$ /C composite (i.e., 46.6, 59.4 and 71 wt.% corresponding to 0.2, 0.35, and 0.4 g of  $\text{Na}_2\text{SnO}_3 \cdot 4\text{H}_2\text{O}$ , respectively), which were labeled as  $\text{SnO}_2$ /C-46,  $\text{SnO}_2$ /C-59 and  $\text{SnO}_2$ /C-71, respectively.

### 2.2. Structure and electrochemical characterization

The morphology and microstructure of the products were obtained using field emission scanning electron microscopy (FE-SEM, JEOL JSM-7401F) and transmission electron microscopy (TEM, JEOL JEM-2010) with a selected area electron diffraction pattern (SAED). The crystal structure and composition were characterized by X-ray diffraction measurement (XRD, Rigaku, D/max-Rbusing Cu K $\alpha$  radiation) and laser. Raman spectroscopy (Renishaw in Via). Thermogravimetric analysis (TGA) of the as-prepared  $\text{SnO}_2$ /C composites were carried out with a thermogravimetric analysis instrument (TGA, SDT Q600 V8.2 Build 100).

Electrochemical measurements were performed using 2016-type coin cells assembled in an argon-filled glove box (German, M. Braun Co.,  $[\text{O}_2] < 1 \text{ ppm}$ ,  $[\text{H}_2\text{O}] < 1 \text{ ppm}$ ). The working electrodes were composed of the active material ( $\text{SnO}_2$ /C), conductive material (acetylene black, AB), and binder (poly-vinylidifluoride, PVDF) in a weight ratio of  $\text{SnO}_2$ /C/AB/PVDF = 70:20:10 and pasted on Cu foil. Pure lithium foil was used as the counter electrode. A glass fiber (GF/A) from Whatman was used as the separator. The electrolyte consisted of a solution of 1 M  $\text{LiPF}_6$  in ethylene carbonate and dimethyl carbonate (EC + DMC) (1:1 in volume). The galvanostatic discharge/charge cycles were carried out on a CT2001a cell test instrument (LAND Electronic Co.) over a voltage range of 0.01–3.0 V at room temperature. Cyclic voltammetry (CV) was implemented on a CHI660D electrochemical workstation at a scan rate of 0.1 mV s<sup>-1</sup> between 0.0 and 3.0 V. For  $\text{SnO}_2$ /C composites working electrode, all the specific capacities reported and current densities used were based on their total mass.

## 3. Results and discussion

The morphology of the as-prepared  $\text{SnO}_2$ /C-59 composite was characterized by using SEM and TEM. We can see from Fig. 1(a) that the composite exhibits a not uniform particle sizes and larger particle sizes reaching over 500 nm. Interestingly, when we observed it using TEM, as shown in Fig. 1(b),  $\text{SnO}_2$  nanoparticles (NPs) (black dots) with uniform particles size were homogeneously embedded in the carbon matrix (gray). In addition, the selected-area electron diffraction (SAED) pattern (inset of Fig. 1(b)) indicates that the  $\text{SnO}_2$  NPs reveal polycrystalline in nature because there are three diffraction rings corresponding to the (110), (101) and (211) planes of polycrystalline  $\text{SnO}_2$ , respectively. It is clearly seen from the high-resolution TEM (HRTEM) (shown in Fig. 1(c)) that the  $\text{SnO}_2$  NPs (indicated by black arrows) have an average size of ca. 6 nm. The visible set of lattice fringes with d-spacing of 0.26 shown in Fig. 1(c) are the characteristic of (101) lattice planes of the rutile  $\text{SnO}_2$ . It should be noted that most of  $\text{SnO}_2$  NPs were wrapped in the carbon matrix rather than exposed on the outer surface and the amorphous carbon (indicated by gray arrows) located in between the  $\text{SnO}_2$  NPs, not only prevents the aggregation of  $\text{SnO}_2$  NPs, but also avoids the exfoliation of  $\text{SnO}_2$  NPs during cycling, as a result, maintaining the integrity of the whole electrode. Fig. 1(d) is the EDS spectrum taken from the as-made sample. The strong peaks for C, Sn and O elements are expected from the carbon matrix,  $\text{SnO}_2$  NPs, respectively. Then, the Si and Cu peaks come from micro-grid used as the sample stage in TEM measurements.

For confirming the excellent electrochemical properties of  $\text{SnO}_2$ /C-59 come from its peculiar architecture, we also prepared other two kinds of composites ( $\text{SnO}_2$ /C-46 and  $\text{SnO}_2$ /C-71) displayed in Fig. 2. The typical size of  $\text{SnO}_2$ /C-46 (the mass of  $\text{Na}_2\text{SnO}_3 \cdot 4\text{H}_2\text{O}$  is 0.2 g) particles is around 50 nm and the particles intimately connected to each other, which could be clearly seen from the SEM (Fig. 2(a)) and TEM images (Fig. 2(b)). The  $\text{SnO}_2$  NPs nanoclusters

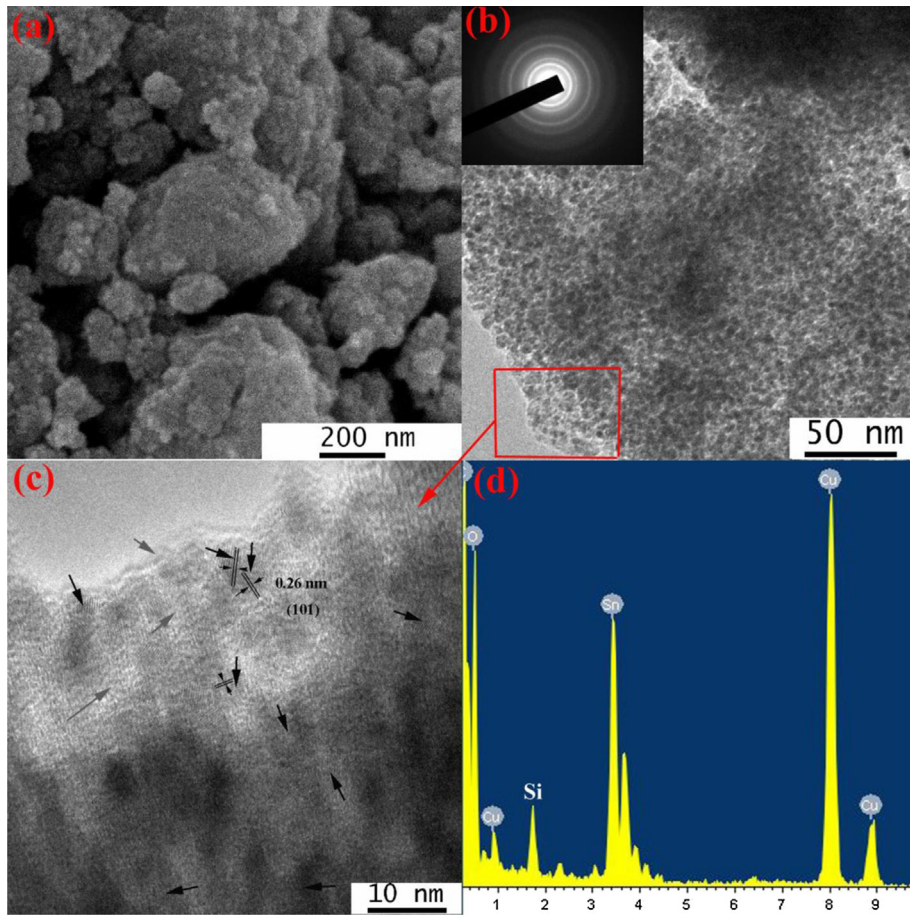


**Fig. 1.** Morphological and compositional characterizations of the  $\text{SnO}_2/\text{C}-59$ : (a) SEM image, (b) TEM image, (c) HRTEM image and SAED pattern (inset), (d) EDS spectrum.

composed of numerous  $\text{SnO}_2$  NPs were mostly coated by ca. 10 nm of a carbon layer indicated by red arrows in Fig. 2(b). When the mass of  $\text{Na}_2\text{SnO}_3 \cdot 4\text{H}_2\text{O}$  increased to 0.4 g, the size of  $\text{SnO}_2/\text{C}-71$  became uneven shown in Fig. 2(c). And compared to  $\text{SnO}_2/\text{C}-59$ , the  $\text{SnO}_2$  NPs of  $\text{SnO}_2/\text{C}-71$  became larger and uneven indicated by red arrows in Fig. 2(d). Furthermore, the  $\text{SnO}_2$  NPs could not completely coated by the carbon layer due to the lack of carbon (the mass of  $\text{Na}_2\text{SnO}_3 \cdot 4\text{H}_2\text{O}$  too much).

Then, we observed the compositional characterizations of different samples by X-ray diffraction measurement, the corresponding XRD patterns are showed in Fig. 3(a). It is clearly seen from the patterns of XRD that all intensive peaks can be well indexed to pure rutile  $\text{SnO}_2$  (JCPDS card no. 41-1445, SG: P42/mnm,  $a_0 = 4.738 \text{ \AA}$ ,  $c_0 = 3.187 \text{ \AA}$ ) [25]. No intensive peak belonging to carbon is detected, indicating the amorphous nature of carbon [26]. This is supported by the Raman spectrum of the  $\text{SnO}_2/\text{C}-59$  composite shown in Fig. 3(b), in which two broad peaks at 1355 and  $1585 \text{ cm}^{-1}$  can be assigned to typical D and G bands of amorphous carbon, respectively [27]. The peak intensity ratio between the D and G bands ( $I_D/I_G$ ) generally provides a useful index for comparing the degree of crystallinity of various carbon materials, i.e., a smaller ratio of  $I_D/I_G$  corresponds to a higher degree of ordering in the carbon material [28]. The  $I_D/I_G$  ratio for  $\text{SnO}_2/\text{C}-59$  estimated to be about 1.4, demonstrating that the carbon formed is fairly amorphous due to the low calcination temperature of  $500^\circ\text{C}$ . The Raman result is in good agreement with the TEM and XRD results, validating the  $\text{SnO}_2$  NPs uniformly embedded in amorphous carbon matrix. In addition, amorphous carbon contains abundant defects

and vacancies, which not only favor the diffusion of lithium ions, but also provide more reversible sites for lithium storage, contributing to the overall capacity [29]. For the application in LIBs of  $\text{SnO}_2/\text{C}$  composite nanomaterials, there is a compromise between cycling performance and lithium storage capacity, since carbon has very limited capacity. Herein, the  $\text{SnO}_2$  content of three kinds of  $\text{SnO}_2/\text{C}$  composites determined from the thermogravimetric analysis (TGA), and the results shown in Fig. 3(c). The remaining  $\text{SnO}_2$  contents of the  $\text{SnO}_2/\text{C}-46$ ,  $\text{SnO}_2/\text{C}-59$ , and  $\text{SnO}_2/\text{C}-71$  are determined to be about 46.4, 59.4, and 71% by weight, respectively, which is consistent with the TEM observation. All of these results mentioned above demonstrate that the as-prepared  $\text{SnO}_2/\text{C}-59$  composite possesses three key advantages of ultrasmall  $\text{SnO}_2$  nanoparticles, uniform distribution, and amorphous carbon matrix comparing to  $\text{SnO}_2/\text{C}-46$  and  $\text{SnO}_2/\text{C}-71$ .

We subsequently investigate the electrochemical properties of the  $\text{SnO}_2/\text{C}-59$  composite as an anode material for LIBs. For proving the excellent electrochemical performance of the  $\text{SnO}_2/\text{C}-59$  composite, we compared it with other composites including our as-prepared other two kinds of composites and the similar  $\text{SnO}_2/\text{C}$ -based composites reported in other literature. Fig. 4(a) shows cyclic voltammograms of the initial 5 cycles of the  $\text{SnO}_2/\text{C}-59$  composite at a scan rate of  $0.1 \text{ mV s}^{-1}$  from 0.0 to  $3.0 \text{ V}$ . There is an obvious reduction peak near  $0.77 \text{ V}$  in the first cathodic scan, which is attributed to the formation of a solid electrolyte interface (SEI) layer and the conversion of  $\text{SnO}_2$  to metallic Sn. This peak shows a significantly drop in current and shifts to higher potential after the first cycle correspond to the conversion reaction only. In

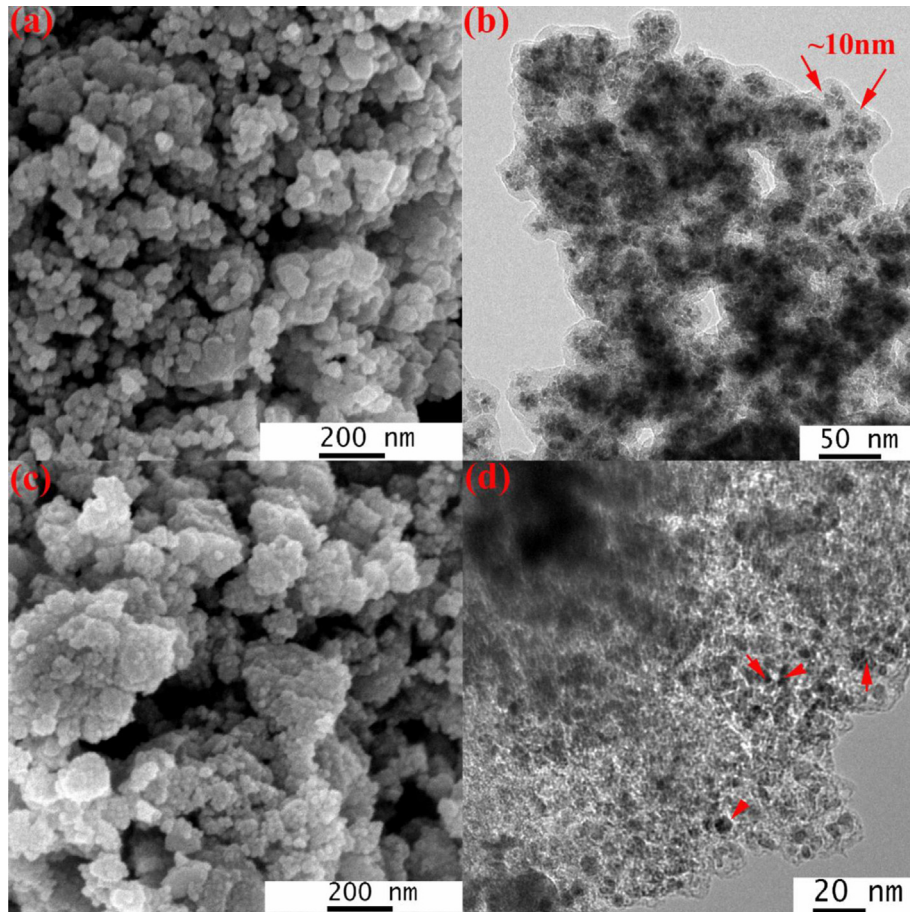


**Fig. 2.** (a) SEM image and (b) TEM image of  $\text{SnO}_2/\text{C-46}$ , (c) SEM image and (d) TEM image of  $\text{SnO}_2/\text{C-71}$ . (For interpretation of the references to colour in this figure legend, the reader is referred to the web version of this article.)

subsequent cycles, two characteristic pairs of redox peaks are clearly observed in the CV curves, locating at 0.03 and 0.6 V and 0.95 and 1.25 V, respectively. The peaks located at ca. 0.95 and ca. 1.25 V still exist even during the fifth cycle, suggesting partial reversibility of the reaction between  $\text{SnO}_2$  and  $\text{Li}^+$  ( $\text{SnO}_2 + 4\text{Li}^+ + 4\text{e}^- \rightarrow \text{Sn} + 3\text{Li}_2\text{O}$ ). This behavior will be beneficial for improving the lithium storage of  $\text{SnO}_2$ -based composites electrodes. Note here, Wang et al. previously reported this phenomenon and found that the partial electrochemical reversibility of  $\text{Li}_2\text{O}$  is able to activate when applied nanosized particles (10–20 nm) with large surface area [8]. The peak located at 1.4 V may attribute to the decomposition of tiny electrolyte. The unchanged peak

current intensity, except the first cycle, indicates good cycling stability of the  $\text{SnO}_2/\text{C-59}$  composite. The voltage profiles of 8 cycles of the  $\text{SnO}_2/\text{C-59}$  corresponding to 1st, 2nd, 5th, 10th, 20th, 100th, 150th and 200th cycle at a current density of  $200 \text{ mA g}^{-1}$  between 0.01 and 3 V, respectively, as shown in Fig. 4(b). In good agreement with its CV behavior, two poorly defined plateau regions can be identified in the first discharge process, and it gives a very high discharge capacity of  $1700 \text{ mAh g}^{-1}$ . In the following charge process delivers a charge capacity of  $1022.8 \text{ mAh g}^{-1}$  and distributes to a Coulombic efficiency of 60.2%. The capacity loss of  $697.2 \text{ mAh g}^{-1}$  in the first cycle is mainly attributed to the formation of SEI film, electrolyte decomposition and so on. It is worth noting that the

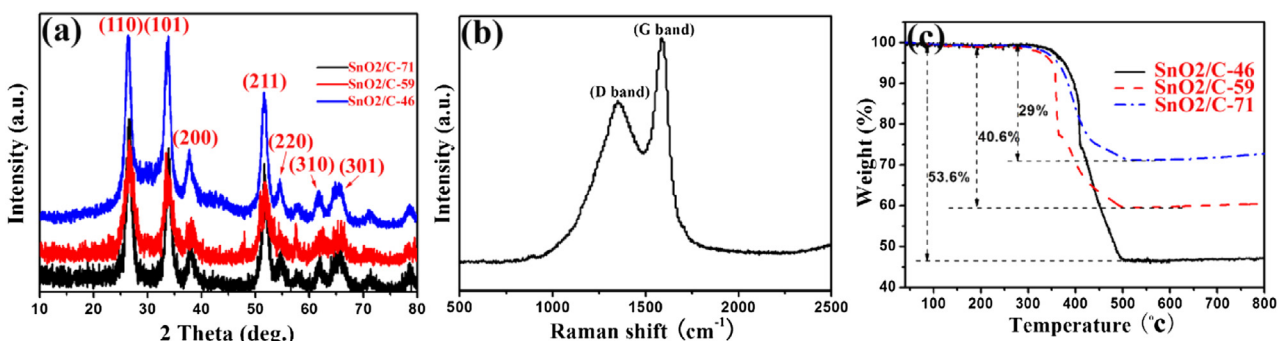


**Fig. 3.** (a) XRD patterns and (b) Raman spectra of  $\text{SnO}_2/\text{C-59}$ , (c) TGA analysis of  $\text{SnO}_2/\text{C-46}$ ,  $\text{SnO}_2/\text{C-59}$  and  $\text{SnO}_2/\text{C-71}$ .

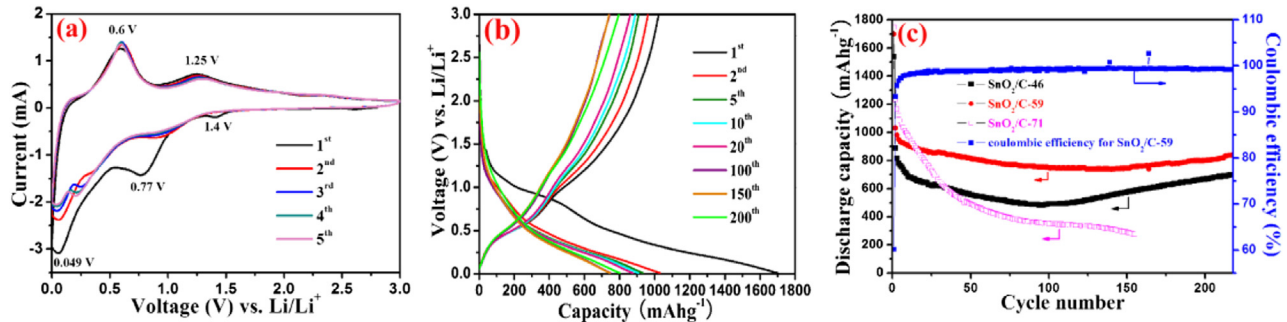


Fig. 4. (a) Representative CVs of the SnO<sub>2</sub>/C-59 at a scan rate of 0.1 mV s<sup>-1</sup> between 0.0 V and 3.0 V, (b) Discharge/charge voltage profiles of the SnO<sub>2</sub>/C-59 at 200 mA g<sup>-1</sup> between 0.01 V and 3.0 V, (c) Comparative cycling performance between SnO<sub>2</sub>/C-59, SnO<sub>2</sub>/C-64 and SnO<sub>2</sub>/C-71 at 200 mA g<sup>-1</sup> between 0.01 V and 3.0 V.

discharge curves in the following cycles almost overlapped with the first one. The repeatable discharge/charge curves after the first cycle demonstrate good cycling stability.

The good electrochemical properties of the SnO<sub>2</sub>/C-59 are mainly due to its unique nanostructure. The composite formed by SnO<sub>2</sub> uniformly dispersed in carbon not only fully utilize the ultrasmall SnO<sub>2</sub> nanoparticles to store lithium ions, but also improve the cycling stability. Fig. 4(c) shows the cycling performance of the SnO<sub>2</sub>/C-59 during discharge/charge process at a current density of 200 mA g<sup>-1</sup> between 0.01 and 3.0 V. The SnO<sub>2</sub>/C-59 composite exhibits exceptional lithium storage performance. It exhibited a high reversible capacity of 839 mAh g<sup>-1</sup> even after 217 cycles. The Coulombic efficiency approaches 99.2%, showing excellent reversibility. It is worth noting that there is a slow decay in the specific capacity before 140th cycle (738.5 mAh g<sup>-1</sup> at 140th cycle) and a subsequent slow increase. The slow increase in the specific capacity during cycling has also been reported in previous studies on metal oxide electrodes [30–34]. The reversible formation of a polymeric gel-like layer by electrolyte decomposition has been suggested as one of the possible reasons for this phenomenon [30–33]. In addition, the activation of active materials may also contribute to the increased capacity. Moreover, Zhou's group have reported that metal or metal oxide (such as Sn and SnO<sub>2</sub>) nanoparticles generated during long-term cycling might serve as electrocatalysts for the reversible conversion of some components of solid electrolyte interface films, providing the metal oxide electrodes with extra capacity [34]. This is in good agreement with our result, in which the capacity starts to increase after 140 cycles as shown in Fig. 4(b) (the discharge capacity is 745 mAh g<sup>-1</sup> at 150th, and then increases to 801.7 mAh g<sup>-1</sup> at 200th).

Then, we also compared the cyclic performances of the SnO<sub>2</sub>/C-59 with SnO<sub>2</sub>/C-46, SnO<sub>2</sub>/C-71 between 0.01 and 3.0 V at 200 mA g<sup>-1</sup> shown in Fig. 4(c). The SnO<sub>2</sub>/C-46 delivers a discharge capacity of 488.4 and 698.9 mAh g<sup>-1</sup> after 100 and 217 cycles, respectively. However, the SnO<sub>2</sub>/C-71 only remains at 275.5 mAh g<sup>-1</sup> in the 155 cycles, indicating the cycling performance of the SnO<sub>2</sub>/C-59 composite is significantly improved. The better lithium storage of SnO<sub>2</sub>/C-46 due to its nanostructure, namely, SnO<sub>2</sub> NPs cluster coated by a thick carbon layer with 10 nm. For SnO<sub>2</sub>/C-71, the larger SnO<sub>2</sub> NPs did not sufficiently coated by carbon, resulting in worse lithium storage. Thus, the SnO<sub>2</sub>/C-59 composite exhibited excellent lithium storage performance and cycling stability due to its peculiar architecture, namely, uniform distribution of ultrasmall SnO<sub>2</sub>, and sufficiently encapsulated by electronic conductivity carbon matrix. In addition, we further compared the lithium storage properties with that of similar composites which have been reported and listed in Table 1. Compared to them, our as-prepared SnO<sub>2</sub>/C-59 composite manifests greatly enhanced lithium storage properties and cycling performance.

The cycling performance of the SnO<sub>2</sub>/C-59 composite was also investigated at high current density. Fig. 5(a) shows the cycling performance of the SnO<sub>2</sub>/C-59 between 0.01 and 3 V at 800 mA g<sup>-1</sup>. It exhibits a reversible capacity of 712.8 mAh g<sup>-1</sup> even after 378 cycles. Moreover, the Coulombic efficiency almost approaches 100%, showing excellent reversibility at high current density. This excellent performance also profited from ultrasmall SnO<sub>2</sub> NPs uniformly distributed in electronic conductivity carbon matrix. Fig. 5(b) illustrates the rate performance of the SnO<sub>2</sub>/C-59 composite at various current densities from 200 to 2000 mA g<sup>-1</sup>. The specific capacities of the composite are 862, 779.9, 679.8, 561.7 and 392.5 mAh g<sup>-1</sup> when cycles at 200, 400, 800, 1600 and 2000 mA g<sup>-1</sup>, respectively. When back to 200 mA g<sup>-1</sup>, a capacity of 791 mAh g<sup>-1</sup> can be restored, indicating the good rate performance and stability of the SnO<sub>2</sub>/C-59 composite. To further confirm the structural integrity of the SnO<sub>2</sub>/C-59 electrode during repeated cycling, we decomposed a cell after 378 cycles at a current density of 800 mA g<sup>-1</sup> and observed the morphology by TEM, as shown in Fig. 6. It can be clearly seen that the nanostructure of Sn or Li<sub>x</sub>Sn nanoparticles embedded in carbon is preserved even after 378

Table 1

Comparison of our product SnO<sub>2</sub>/C-59 with SnO<sub>2</sub>/C-based anode materials reported in other literature.

SnO <sub>2</sub> -C-based anode materials	Potential cutoff (V)	Current density (mA g <sup>-1</sup> )	Cycles	Capacity (mAh g <sup>-1</sup> )	Reference
Our product SnO <sub>2</sub> /C-59	3–0.01	200	217	839	This work
Our product SnO <sub>2</sub> /C-59	3–0.01	800	378	712.8	This work
SWNTS@SnO <sub>2</sub> @PPy	3–0.05	150	100	823	[1]
CNTs@SnO <sub>2</sub> @C	2–0.01	100	65	462.5	[2]
SnO <sub>2</sub> NS-graphene	1.2–0.01	400	50	518	[20]
SnO <sub>2</sub> NPs in CNTs	2.5–0.005	50	50	560	[21]
SnO <sub>2</sub> @C nanochains	2–0.005	300	100	646	[22]
SnO <sub>2</sub> /Graphene	1.5–0.005	100	20	433	[24]
SnO <sub>2</sub> /mesoporous carbon	2–0.01	100	50	473	[35]
SnO <sub>2</sub> /SWCNHs	3–0.05	500	180	530	[16]
SnO <sub>2</sub> HPNFs	3–0.01	100	50	583	[13]
SnO <sub>2</sub> HPNTs	3–0.01	100	50	645	[13]
SnO <sub>2</sub> @C yolk–shell	3–0	100	100	630	[36]
RHC-SnO <sub>2</sub> –C	2–0.05	50	80	525	[37]
Dense SnO <sub>2</sub> /C	3–0	100	50	630	[38]
SnO <sub>2</sub> on PANI@RGO	3–0.001	0.2C	50	573.6	[39]
SnO <sub>2</sub> nanorods/GS	3–0	300	50	574.6	[40]
SnO <sub>2</sub> /GNS	2–0.05	50	30	570	[41]
MWCNT/SnO <sub>2</sub>	3–0	156	100	420	[42]
SnO <sub>2</sub> -80@CMK-5	3–0.005	400	100	1004	[43]
SnO <sub>2</sub> /graphene	2–0.005	0.2C	100	550	[44]
SnO <sub>2</sub> NSs-array film	1.2–0.01	391	50	674.9	[45]
Reduced GO/SnO <sub>2</sub>	3–0.01	100	200	718	[46]
SnO <sub>2</sub> @C/graphene	3–0.01	100	50	1015	[47]
SnO <sub>2</sub> /C hollow spheres	2–0.005	100	50	473	[48]

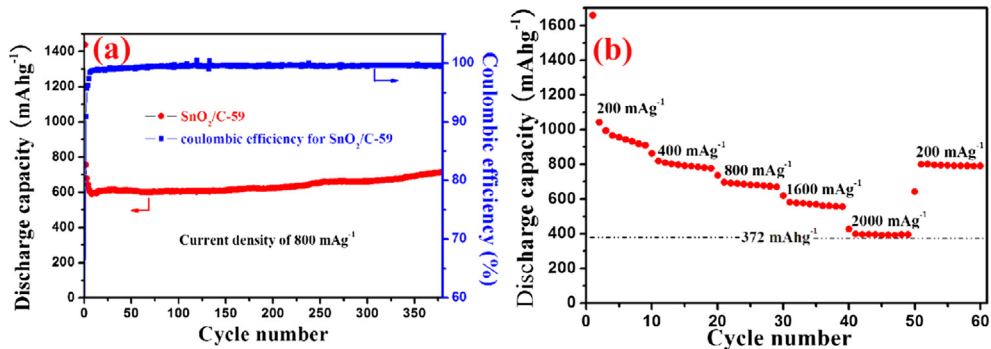


Fig. 5. (a) Cycling performance of the SnO<sub>2</sub>/C-59 between 0.01 V and 3.0 V at 800 mA g<sup>-1</sup>, (b) Rate performance of the SnO<sub>2</sub>/C-59.

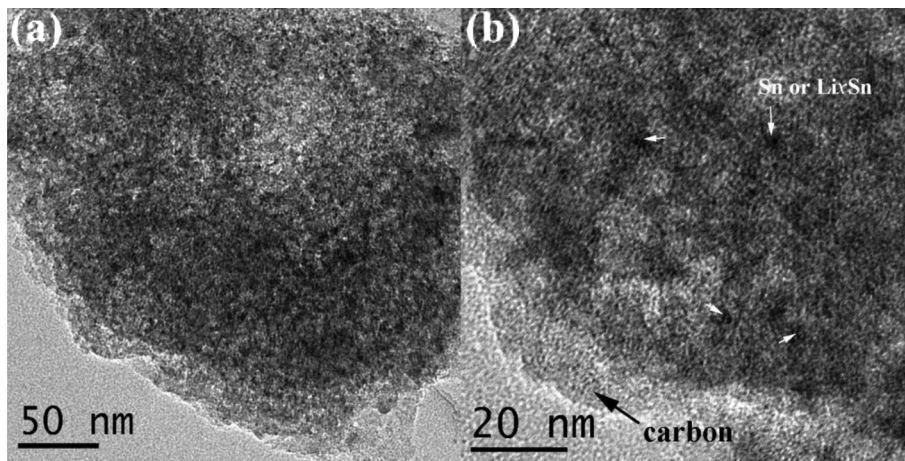


Fig. 6. (a) TEM and (b) magnified TEM images of the SnO<sub>2</sub>/C-59 after 378 cycles at 800 mA g<sup>-1</sup>.

cycles, determining the good stability of this composite during repeated discharge/charge cycles. In a word, the superior cycling performance has been proven is attributed to three unique features of the SnO<sub>2</sub>/C-59 composite. First is the ultrasmall size of SnO<sub>2</sub> NPs. It has been shown that reduced particle size can significantly reduce the strain and improve the electrochemical property of electrode materials. Second, the carbon matrix, which acts to release strain, can effectively buffers the large volume change and prevents nanoparticles aggregation over repeated discharge/charge process. Finally, the uniform distribution of SnO<sub>2</sub> NPs in carbon matrix is a key factor to generate a balanced stress over the whole composite particles and electrode, thus improving long-term electrochemical performance.

#### 4. Conclusions

In summary, we have successfully prepared SnO<sub>2</sub>/C-59 composite by using a facile strategy, namely, a simple hydrothermal and subsequent carbonization approach. In this composite, ultrasmall SnO<sub>2</sub> with uniform size of ca. 6 nm are homogeneously embedded in carbon matrix. The peculiar architecture can effectively alleviate stress and accommodate large volume changes, as well as prevent the pulverization and agglomeration of SnO<sub>2</sub> NPs upon prolonged cycling. As a result, when tested as potential anode materials for LIBs, the SnO<sub>2</sub>/C-59 composite showed a reversible capacity of 839.1 mAh g<sup>-1</sup> at 200 mA g<sup>-1</sup> after 217 cycles. More importantly, 712.8 mAh g<sup>-1</sup> can be obtained at a high current density of 800 mA g<sup>-1</sup> even after 378 cycles. Thus, the as-prepared SnO<sub>2</sub>/C-59 composite exhibited excellent lithium storage capacity and cycling

performance, which are largely due to the unique integration of ultrasmall SnO<sub>2</sub>, uniform distribution and elastic amorphous carbon. Meanwhile, the synthesis of SnO<sub>2</sub>/C-59 is simple, making this composite very promising and attractive as an anode material for lithium-ion batteries.

#### Acknowledgments

We are grateful for financial support from the National Natural Science Foundation of China (Grant no. 21103108 and 21173148) and materials characterization from Instrumental Analysis Center of Shanghai Jiao Tong University.

#### References

- Y. Zhao, J. Li, N. Wang, C.X. Wu, G.F. Dong, L.H. Guan, *J. Phys. Chem. C* **116** (2012) 18612.
- P. Wu, N. Du, H. Zhang, J.X. Yu, D.R. Yang, *J. Phys. Chem. C* **114** (2010) 22535–22538.
- P. Wu, N. Du, H. Zhang, J.X. Yu, Y. Qi, D.R. Yang, *Nanoscale* **3** (2011) 746–750.
- P. Nie, L.F. Shen, H.F. Luo, B. Ding, G.Y. Xu, J. Wang, X.G. Zhang, *J. Mater. Chem. A* **2** (2014) 5852–5857.
- X.W. Lou, C.M. Li, L.A. Archer, *Adv. Mater.* **21** (2009) 2536.
- C. Kim, M. Noh, M. Choi, J. Cho, B. Parl, *Chem. Mater.* **17** (2005) 3297.
- S.M. Paek, E. Yoo, I. Honma, *Nano Lett.* **9** (2009) 72.
- C. Wang, G.H. Du, K. Stahl, H.X. Huang, Y.J. Zhong, J.Z. Jiang, *J. Phys. Chem. C* **116** (2012) 4000–4011.
- S.J. Ding, X.W. Lou, *Nanoscale* **3** (2011) 3586.
- J.Z. Wang, N. Du, H. Zhang, J.X. Yu, D.R. Yang, *J. Phys. Chem. C* **115** (2011) 11302.
- J. Pan, X.F. Song, J. Zhang, H. Shen, Q.H. Xiong, *J. Phys. Chem. C* **115** (2011) 22225.

- [12] J.P. Liu, Y.Y. Li, X.T. Huang, R.M. Ding, Y.Y. Hu, J. Jiang, L. Liao, *J. Mater. Chem.* 19 (2009) 1859.
- [13] T. Yang, B.G. Lu, *Phys. Chem. Chem. Phys.* 16 (2014) 4115.
- [14] Y. Wang, H.C. Zeng, J.Y. Lee, *Adv. Mater.* 18 (2006) 645.
- [15] P. Wu, N. Du, H. Zhang, C. Zhai, D. Yang, *ACS Appl. Mater. Interfaces* 3 (2011) 1946–1952.
- [16] Y. Zhao, J. Li, Y. Ding, L. Guan, *RSC Adv.* 1 (2011) 852–856.
- [17] L. Wang, D. Wang, H.Z. Dong, F.X. Zhang, J. Jin, *Nano Lett.* 13 (2013) 1711–1716.
- [18] G. Derrien, J. Hassoun, S. Panero, B. Scrosati, *Adv. Mater.* 19 (2007) 2336–2340.
- [19] Q.H. Tian, Z.X. Zhang, J.Z. Chen, L. Yang, S.I. Hirano, *J. Power Sources* 246 (2014) 587–595.
- [20] S.J. Ding, D.Y. Luan, F.Y.C. Boey, J.S. Chen, X.W. Lou, *Chem. Commun.* 47 (2011) 7155.
- [21] X. Liu, M.H. Wu, M.R. Li, X.L. Pan, J. Chen, X.H. Bao, *J. Mater. Chem. A* 1 (2013) 9527–9535.
- [22] X.Y. Yu, S.Y. Yang, B.H. Zhang, D. Shao, X.M. Dong, Y.P. Fang, Z.S. Li, H.Q. Wang, *J. Mater. Chem.* 21 (2011) 12295–12302.
- [23] J.P. Li, P. Wu, Y. Ye, H. Wang, Y.M. Zhou, Y.W. Tang, T.H. Lu, *CrystEngComm* 16 (2014) 517–521.
- [24] J.F. Liang, W. Wei, D. Zhong, Q.L. Yang, L.D. Li, L. Guo, *ACS Appl. Mater. Interfaces* 4 (2012) 454–459.
- [25] S.J. Ding, J.S. Chen, G.G. Qi, X.N. Duan, Z.Y. Wang, E.P. Giannelis, L.A. Archer, X.W. Lou, *J. Am. Chem. Soc.* 133 (2011) 21–23.
- [26] D. Deng, J.Y. Lee, *Angew. Chem. Int. Ed.* 48 (2009) 1660.
- [27] J. Hwang, S.H. Woo, J. Shim, C. Jo, K.T. Lee, J. Lee, *ACS Nano* 7 (2013) 1036.
- [28] T. MuraliGanth, K.R. Stroukoff, A. Manthiram, *Chem. Mater.* 22 (2010) 5758.
- [29] Z.Q. Zhu, F.Y. Cheng, J.J. Chen, *J. Mater. Chem. A* 1 (2013) 9484.
- [30] Z. Wang, D. Luan, S. Madhavi, Y. Hu, X.W. Lou, *Energy Environ. Sci.* 5 (2012) 5252.
- [31] G. Zhou, D.W. Wang, F. Li, L. Zhang, N. Li, Z.S. Wu, L. Wen, G.Q. Lu, H.M. Cheng, *Chem. Mater.* 22 (2010) 5306.
- [32] S. Laruelle, S. Grigeon, P. Poizot, M. Dolle, L. Dupont, J.M. Tarascon, *J. Electrochem. Soc.* 149 (2002) A627.
- [33] S.L. Chou, J.Z. Wang, D. Wexler, K. Konstantinov, C. Zhong, H.K. Liu, S.X. Dou, *J. Mater. Chem.* 20 (2010) 2092.
- [34] L.W. Su, Z. Zhou, P.W. Shen, *J. Phys. Chem. C* 116 (2012) 23974.
- [35] L. Chen, P. Wu, H. Wang, Y. Ye, B. Xu, G.P. Cao, Y.M. Zhou, T.H. Lu, Y.S. Yang, *J. Power Sources* 247 (2014) 178–183.
- [36] J.X. Wang, W. Li, F. Wang, Y.Y. Xia, A.M. Asirib, D.Y. Zhao, *Nanoscale* 6 (2014) 3217–3222.
- [37] Y. Li, S.M. Zhu, Q.L. Liu, J.J. Gu, Z.P. Guo, Z.X. Chen, C.L. Feng, D. Zhang, W.J. Moon, *J. Mater. Chem.* 22 (2012) 2766–2773.
- [38] J. Liu, W. Li, A. Manthiram, *Chem. Commun.* 46 (2010) 1437–1439.
- [39] R.L. Liang, H.Q. Cao, D. Qian, J.X. Zhang, M.Z. Qu, *J. Mater. Chem.* 21 (2011) 17654–17657.
- [40] C.H. Xu, J. Sun, L. Gao, *J. Mater. Chem.* 22 (2012) 975–979.
- [41] S.M. Paek, E.J. Yoo, I. Honma, *Nano Lett.* 9 (2009) 72–75.
- [42] Y.H. Jin, K.M. Min, S.D. Seo, H.W. Shim, D.W. Kim, *J. Phys. Chem. C* 115 (2011) 22062–22067.
- [43] F. Han, W.C. Li, M.R. Li, A.H. Lu, *J. Mater. Chem.* 22 (2012) 9645–9651.
- [44] M. Zhang, D.N. Lei, Z.F. Du, X.M. Yin, L.B. Chen, Q.H. Li, Y.G. Wang, T.H. Wang, *J. Mater. Chem.* 21 (2011) 1673–1676.
- [45] X.Y. Zhao, B. Liu, C.W. Hu, M.H. Cao, *Chem. Eur. J.* 19 (2013) 1–8.
- [46] X.W. Guo, X.P. Fang, Y. Sun, L.Y. Shen, Z.X. Wang, L.Q. Chen, *J. Power Sources* 226 (2013) 75–81.
- [47] P.C. Lian, J.Y. Wang, D.D. Cai, L.X. Ding, Q.M. Jia, H.H. Wang, *Electrochim. Acta* 116 (2014) 103–110.
- [48] X.W. Lou, D. Deng, J.Y. Lee, L.A. Archer, *Chem. Mater.* 20 (2008) 6562–6566.